EPJ manuscript No.
(will be inserted by the editor)

Nickel isotopes in stellar matter

Jameel-Un Nabi[1,2]
[1] Faculty of Engineering Sciences, GIK Institute of Engineering Sciences and Technology, Topi 23640, Swabi, Khyber Pakhtunkhwa, Pakistan
[2] The Abdus Salam ICTP, Strada Costiera 11, 34014, Trieste, Italy

arXiv:1408.4322v1 [nucl-th] 19 Aug 2014

the date of receipt and acceptance should be inserted later

Abstract. Isotopes of nickel play a key role during the silicon burning phase up to the presupernova phase of massive stars. Electron capture rates on these nickel isotopes are also important during the phase of core contraction. I present here the microscopic calculation of ground and excited states Gamow-Teller (GT) strength distributions for key nickel isotopes. The calculation is performed within the framework of pn-QRPA model. A judicious choice of model parameters, specially of the Gamow-Teller strength parameters and the deformation parameter, resulted in a much improved calculation of GT strength functions. The excited state GT distributions are much different from the corresponding ground-state distributions resulting in a failure of the Brink's hypothesis. The electron capture and positron decay rates on nickel isotopes are also calculated within the framework of pn-QRPA model relevant to the presupernova evolution of massive stars. The electron capture rates on odd-A isotopes of nickel are shown to have dominant contributions from parent excited states during as early as silicon burning phases. Comparison is being made with the large scale shell model calculation. During the silicon burning phases of massive stars the electron capture rates on ^{57,59}Ni are around an order of magnitude bigger than shell model rates and can bear consequences for core-collapse simulators.

PACS. 2 3.40.-s β-decay; double β-decay; electron and muon capture - 26.30.Jk Weak interaction and neutrino induced processes, galactic radioactivity - 26.50.+x Nuclear physics aspects of supernovae - 21.60.Jz Nuclear Density Functional Theory and Extensions

1 Introduction

Collective excitation properties of nuclei at finite temperature is of great utility in astrophysical environments. Of special mention is the behavior of charge-exchange transitions in hot nuclei. The Gamow-Teller (GT) transition is one of the most important nuclear weak processes of the spin-isospin ($\sigma\tau$) type. Ikeda, Fujii and Fujita [1] predicted the GT resonance in 1962 which was later discovered by the Indiana group using the (p,n) reaction [2]. Since then the interest in the study of spin-isospin symmetry and the GT strength properties of the nuclei increased manyfold (see for example the review article by Ref. [3]).

The GT properties of nuclei in the medium mass region are main prerequisites to study the presupernova evolution of massive stars [4]. Throughout this paper massive stars imply stars with mass $M \geq 10M_{\odot}$. As soon as the core of a massive star exceeds the appropriate Chandrasekhar mass, electrons are captured by nuclei in stellar matter and the electron capture rate is a crucial factor that determines the initial collapse phase. The GT_+ transitions contribute significantly in the determination of electron capture rates during the presupernova phase of massive stars. In the GT_+ strength, a proton is changed into a neutron (the plus sign is for the isospin raising operator (t_+), present in the GT matrix elements, which converts a proton into a neutron). In many collapse simulations the GT_+ strength was assumed to reside in a single resonance and the strength of this resonance was determined from the single-particle model [5]. The approximation was done mainly due to insufficient experimental information and rather limited theoretical and computational advancements prevailing at the time. Since then considerable progress was made, both in the theoretical and experimental side, which led to a better understanding of the nuclear structure. Aufderheide and collaborators [6] showed that a strong phase space dependence makes the relevant electron capture rates more sensitive to GT distributions than to total GT strengths. The (n,p) experiments on the other side revealed the fact that the GT_+ strength is fragmented over many states, and that the total strength is quenched compared to single-particle model. Microscopic calculations of GT_+ strength functions and weak-interaction rates in stellar matter were then performed successfully using the pn-QRPA model (e.g. [7]) and the shell model (e.g. [8]).

Isotopes of nickel play inarguably a crucial role in the presupernova evolution of massive stars. Many simulation studies of presupernova evolution of massive stars showed electron capture rates on nickel isotopes to considerably alter the lepton-to-baryon rate of change of the stellar core (e.g. [9,10]). Aufderheide and collaborators [9] also showed the β-decay on few neutron-rich nickel isotopes to affect the lepton-to-baryon ratio of stellar core. However these β-decays were orders of magnitude smaller than electron capture rates and were not considered important for presupernova evolution of massive stars by Heger and collaborators [10]. Electron capture rates on ^{56,57,58,59,60,61,63,64,65}Ni were considered important from previous simulation studies of core-collapse. The GT_+ strength distribution and electron capture rates on ^{56}Ni were discussed in detail earlier [11]. In this paper I would like to report on the improved calculation of the GT_+ strength functions and associated electron capture rates on nickel isotopes (mass number 57 to 65) using the pn-QRPA as the base model. The paper is written as follows. Section 2 briefly discusses the pn-QRPA model and presents the calculations of GT_+ strength functions and electron capture rates on these nickel isotopes. The results are compared with the large scale shell model results in Section 3. Conclusions are given in Section 4.

2 The nuclear model and results

The pn-QRPA model was first developed by Halbleib and Sorensen [12]. The extension of the original model to deformed nuclei was first given by Krumlinde and Möller [13] and to excited state contributions by Muto and collaborators [14]. The model was then adapted to calculate stellar weak rates (see for example [7]). Two important parameters of the pn-QRPA model are the GT strength parameters and the deformation parameter. Special emphasis was given in the current project to smartly choose these key model parameters. The Hamiltonian of the model was taken to be of the form:

$$H^{QRPA} = H^{sp} + V^{pair} + V^{ph}_{GT} + V^{pp}_{GT}. \quad (1)$$

The single particle energies and wave functions were calculated in the Nilsson model (which takes into account nuclear deformations). The BCS model was used to calculate the pairing force. In the pn-QRPA formalism, proton-neutron residual interactions occur as particle-particle (pp) and particle-hole (ph) interaction. The pp interaction is of paramount importance for electron capture and positron decay rate calculation [15,16]. Both pp and ph interaction terms are given a separable form in the model and are characterized by two interaction constants (χ for the ph force and κ for the pp force). The calculation of β-decay half-lives depends heavily on the choice of these interaction parameters [15,16]. In order to improve the calculation a fine-tuning of these strength parameters was performed for the nickel isotopes (mass number 50 to 94). Experimental values are available in literature for the centroids and total GT strength for the even-even isotopes of nickel, ^{58,60,62,64}Ni. The idea was to find the optimal value of χ and κ that best reproduced the measured values for these even-even isotopes of nickel. For ^{58}Ni experimental data was taken from [17,18,19,20,21], for ^{60}Ni from [17,18,22], for ^{62}Ni from [18,22] and finally for the case of ^{64}Ni measured values were taken from [18,23,24]. The optimum value for χ and κ was chosen to be 0.001 MeV and 0.052 MeV,

respectively. These parameters were then fixed for the calculation of GT strength functions and associated weak rates for all nickel isotopes. As mentioned earlier deformation of nuclei was taken into account in the current calculation. The deformation parameter is yet another key pn-QRPA model parameter (see also [25]). For the case of even-even isotopes, the experimentally adopted value of the deformation parameters, extracted by relating the measured energy of the first 2^+ excited state with the quadrupole deformation, was taken from Raman et al. [26]. For the case of odd-A nickel isotopes the deformation of the nucleus was calculated as

$$\delta = \frac{125(Q_2)}{1.44(Z)(A)^{2/3}}, \tag{2}$$

where Z and A are the atomic and mass numbers, respectively and Q_2 is the electric quadrupole moment taken from Ref. [27]. Q-values were taken from the mass compilation of Audi et al. [28].

Once the model parameters were carefully chosen, the pn-QRPA model was used for the calculation of GT strength distributions (both ground and excited states), electron capture and positron decay rates in stellar matter. The use of a separable interaction assisted in the incorporation of a luxurious model space of 6 major oscillator shells. The basic formalism for the calculation of electron capture and positron decay rates in the pn-QRPA model can be seen in detail from Ref. [29]. Around 300 parent excited states and as many daughter excited states were considered in the current calculation covering an energy range of up to 15-20 MeV. Each state was treated as a resonance state having a finite band-width of 0.044 MeV for the even-even isotopes and 0.054 MeV for the odd-A isotopes. The GT strength distribution was calculated for all these 300 states in a microscopic fashion. The total electron capture (ec) and positron decay (pd) rate per unit time per nucleus was calculated as

$$\lambda^{ec(pd)} = \sum_{ij} P_i \lambda_{ij}^{ec(pd)}, \tag{3}$$

where P_i is the probability of occupation of parent excited states and follows the normal Boltzmann distribution and λ_{ij} are the partial rates. After the calculation of all partial rates for the transition $i \rightarrow j$ the summation was carried out over all initial and final states until satisfactory convergence was achieved in the rate calculation. An average quenching factor of 0.6 was adopted in the current calculation.

Table 1 shows the value of the deformation parameter for the nickel isotopes used in the current calculation. Shown also are the total calculated GT strength in both (electron capture and β-decay) directions, $\Sigma S_{\beta^{\pm}}$. The sum is taken up to 12 MeV in daughter nuclei. It can be seen from Table 1 that Ikeda sum rule was satisfied in the calculation (small difference arise due to the fact that cutoff energy is taken to be 12 MeV here and also due to some rounding errors).

Since the calculations of stellar electron capture and positron decay rates depend primarily on the calculation of B(GT$_+$) strength distributions, I present here the comparison of measured B(GT$_+$) strength distributions of nickel isotopes (^{58,60,62,64}Ni) with the calculated distributions. The measured values of B(GT$_+$) strength, till 8 MeV in daughter, for ^{58}Ni, ^{60}Ni, ^{62}Ni and ^{64}Ni, is 3.8 $\pm$ 0.4, 3.11 $\pm$ 0.08, 2.53 $\pm$ 0.07 and 1.72 $\pm$ 0.09, respectively [18]. This is to be compared with the pn-QRPA calculated values of 6.95, 5.83, 3.58 and 1.77, respectively. Authors in [22] also calculated the experimentally determined value of B(GT$_+$) strength for ^{60}Ni (^{62}Ni), up to 2.4 (2.3)MeV in ^{60}Co (^{62}Co) to be 1.34 $\pm$ 0.22 (1.28 $\pm$ 0.29). This is to be compared with the pn-QRPA calculated value of 2.89 and 1.63, respectively.

Table 2 shows the values of pn-QRPA calculated centroids for the B(GT$_+$) strength distributions of nickel isotopes. For comparison the values of centroids calculated by LSSM [8] and those by Pruet and Fuller [30] are also shown (where available). The values in column 3 and 4 were adapted from Ref. [30]. Experimental centroids for the even-even isotopes of nickel are given in the last column. With the exception of ^{62}Ni, the pn-QRPA calculated centroids are in reasonable comparison with the measured values. The pn-QRPA model does not exactly reproduce the measured data. However the fair comparison of the calculated centroids and total strength functions (which control the calculated electron capture and positron decay rates) with the measured data does indicate that the nuclear model employed in this calculation should represent a fair estimate of weak rates in stellar matter where no experimental data is available and where the overall physics is rather poorly understood. It is hoped that this calculation could prove beneficial for core-collapse simulators world-side.

Figures 1–3 show the ground state B(GT$_+$) strength distributions for the isotopes of nickel. Figure 1 shows the calculated ground state B(GT$_+$) strength functions for ^{57,58,59}Ni. The abscissa represents energy in daughter ^{57,58,59}Co. Experimental data were incorporated in the calculation wherever possible. The calculated excitation energies were replaced with measured levels when they were within 0.5 MeV of each other. Missing measured states were inserted and inverse transitions (along with their logft values) were also taken into account. No theoretical levels were replaced with the experimental ones beyond the excitation energy for which experimental compilations had no definite spin and/or parity. No forbidden transitions were calculated in this project. Work is currently underway to calculate these transitions. It can be seen from Figure 1 that the model calculates many high-lying transitions in ^{57}Co (calculated

centroid is around 7.25 MeV). The model calculates low-lying GT transitions in ^{58}Co (except for the peak at 7.96 MeV) and locates the centroid at 3.57 MeV. Two big transitions at 4.69 MeV and 9.36 MeV in ^{59}Co moves the B(GT$_+$) centroid at 5.63 MeV for the case of ^{59}Ni. Figure 2 shows the calculated strength functions for ^{60,61,62}Ni. Prominent peaks are seen at 5.41 MeV, 6.85 MeV and 2.81 MeV in daughter ^{60}Co, ^{61}Co and ^{62}Co, respectively. The calculated GT strength functions for ^{63,64,65}Ni are shown in Figure 3. Here much of the strength lies in the low-energy range in daughter nuclei. It can be seen from Figures 1–3 that the GT strength in daughter nuclei is well fragmented. The excited state B(GT$_+$) strength functions were also calculated in a microscopic fashion and are not shown here due to space limitations. These are seen to be much different from the ground state distributions and imply that the Brink's hypothesis is not a good approximation to use in calculation of stellar weak rates for nickel isotopes (Brink's hypothesis states that GT strength distribution on excited states is *identical* to that from ground state, shifted *only* by the excitation energy of the state). It would be shown later that electron captures on nickel isotopes have significant contributions from these excited states during the presupernova and core contraction phases of massive stars. Further electron capture rate on odd-A isotopes of nickel, ^{57,59,61,63}Ni, have dominant contributions from parent excited states during as early as silicon burning phases. The ASCII files for the B(GT$_\pm$) strength distributions for ground and all excited states of nickel isotopes can be requested from the author.

The pn-QRPA calculated electron capture and positron decay rates of nickel isotopes are shown in Figures 4–5. Figure 4 depicts the electron capture and positron decay rates of ^{57,58,59,60}Ni as a function of stellar temperature and density. The electron capture rates are shown for density scale $\rho = 10^{7,8,9,10}$ gcm^{-3}. T$_9$ gives the stellar temperature in units of 10^9 K. The temperature and density scale chosen are pertinent to silicon burning phase to core contraction phase of massive stars. The calculated positron decay rates are independent of stellar density and much smaller than competing electron capture rates. It can be seen from Figure 4 that electron capture rate increases both with increasing stellar density and with increasing stellar temperature. The centroid for the GT$_+$ strength distribution shifts to lower excitation energy in daughter nucleus with increasing nuclear temperature. As density increases the fraction of electrons with energy sufficient for excitation of the GT$_+$ resonance increases in the electron gas. The positron decay rates on even-even isotopes of nickel, ^{58,60}Ni are smaller than ^{57,59}Ni by many orders of magnitude. Except for the case of ^{57}Ni (during the silicon burning phases), the positron decay rates can be safely neglected in comparison to the electron capture rates by simulators. Figure 5 shows corresponding weak-interaction rates for the case of ^{61,63,64,65}Ni. Electron capture rates on ^{62}Ni are not considered important from previous simulation results and are as such not presented here (interested readers can request these rates from the author). For the isotopes of nickel, ^{61,63,64,65}Ni, once again it is seen that the positron decay rates are much smaller and may be neglected in simulation codes compared with the competing electron capture rates. The electron capture rates increase with increasing temperature and density for reasons mentioned above. The complete set of electron capture and beta decay rates on a detailed temperature-density grid point (suitable for interpolation purposes and simulation codes) for nickel isotopes can be requested from the author.

In order to analyze the contribution of the parent excited states to the total rates, the ratio of ground state capture rates to total capture rates, $R_{ec}(G/T)$, was calculated for the nickel isotopes. Table 3 shows this contribution at a selected density scale of $\rho = 10^{8.5}$ gcm^{-3} as a function of increasing stellar temperature. Similar results were obtained for lower densities (pertaining to silicon burning phases) and higher densities (pertaining to presupernova and core contraction phases). It can be seen from Table 3 that for the odd-A nickel isotopes, ^{57,59,61,63}Ni, excited states have dominant contribution at T$_9 \geq$ 3K.

To explain further I take the sample case of ^{57}Ni. Here the first excited state is located at 0.77 MeV. For the ground state the calculated values of the GT strength in electron capture direction, ΣS_{β^+}, and the centroid is 9.98 and 7.25 MeV, respectively (up to 12 MeV in daughter). For the first excited state the calculated corresponding values are 10.9 and 6.73 MeV, respectively. (A similar comparison of pn-QRPA calculated ground and excited states GT strength distributions for iron isotopes were shown earlier in Table 2 of Ref. [31]). The effect of lowering of centroid and increased total strength causes a considerable enhancement in calculated electron capture rate from this first excited state. At a temperature of 3 GK, the calculated value of electron capture rate from ground state is 0.35 s^{-1} whereas the product of electron capture rate and occupation probability of the state gives a total value of 0.33 s^{-1}. For the same temperature, the calculated value of electron capture rate from the first excited state is 5.75 s^{-1} and the product of electron capture rate and occupation probability for the first excited state is 0.28 s^{-1}. This means that alone the first excited state is contributing an additional 85% of the ground state capture rate to the cumulated capture rate. The total electron capture rate from all parent excited states is 0.71 s^{-1} and the ratio of ground state capture rate to total capture rate is thus 0.47. Taking the case of ^{58}Ni (as a sample case for even-even isotope, at the same temperature of 3 GK), the pn-QRPA calculated ground state electron capture rate is 0.291 s^{-1}, the contribution from first excited state (at 1.45 MeV) is 0.00133 s^{-1}. The total electron capture rate is 0.293 s^{-1} and the ratio of ground to total capture rate comes out to be 0.995.

At still higher stellar temperature of T$_9$ = 30K, excited state rates contribute heavily for all isotopes of nickel (as can be seen from Table 3). As mentioned earlier all excited state GT strength distributions were calculated in a microscopic fashion within the framework of the pn-QRPA model and were significantly different from their ground-

state counterparts. The details of the microscopic calculation of ground and excited state GT strength distributions using the pn-QRPA model and phase space calculations can be seen from Ref. [7].

Figure 6 shows the calculated half-lives for nickel isotopes as a function of stellar temperature at a selected density of $\rho = 10^{8.5}$ gcm^{-3}. The total half-lives include contribution from both electron capture and positron decay rates. The lower panel shows the calculated half-lives for ^{57,58,59,60}Ni whereas the upper panel displays the calculated half-lives for ^{61,62,63,64,65}Ni. The calculated half-lives decrease as stellar temperature increases as expected since the electron capture rates increases substantially with increasing temperatures (see Fig. 4 and Fig. 5). The half-life of ^{64}Ni decreases by roughly 50 orders of magnitude as the stellar temperature increases. This is primarily due to an increase in the electron capture rates on ^{64}Ni of similar magnitude as stellar temperature increases.

In the next section I discuss how the pn-QRPA calculation compares with the large scale shell model calculation for the astrophysically important odd-A isotopes of nickel. This comparison might be of special interest for core-collapse simulators.

3 Comparison with shell model

Table 4 compares the pn-QRPA calculated electron capture rate on ^{57}Ni with the large scale shell model calculation (LSSM) [8]. All rates are given in units of s^{-1}. The pn-QRPA calculated electron capture rates on ^{57}Ni are generally bigger than those calculated by LSSM. During the silicon burning phases of massive stars the pn-QRPA calculated electron capture rates are bigger by more than a factor of 6. The pn-QRPA model calculated a total strength of magnitude 9.98 with a centroid around 7.25 MeV in daughter ^{57}Co. At a stellar density of $\rho = 10^7$ gcm^{-3} and a temperature of $T_9 = 5$K (these physical conditions apply roughly to the silicon burning phases of massive stars), the ground state contributes only about 10% to the total electron capture rate. The remaining contribution comes from excited states. As mentioned earlier Brink's hypothesis was not assumed in the current calculation and all excited state contributions were calculated in a microscopic fashion. At higher densities, $\rho \sim 10^9 - 10^{10}$ gcm^{-3}, relevant to presupernova phase, the comparison improves.

The pn-QRPA electron capture rates on ^{59}Ni are also bigger by up to a factor 7 at low densities, $\rho \sim 10^7 - 10^8$ gcm^{-3} (see Table 5). Collapse simulators should again note that the pn-QRPA calculated electron capture rates on ^{59}Ni are around an order of magnitude bigger compared to LSSM rates during the silicon burning phases of massive stars. At higher stellar densities the two calculations are in excellent comparison.

The two calculations are in good comparison for the case of electron captures on ^{61}Ni as can be seen from Table 6. During the presupernova phase (densities around $\rho = 10^{10}$ gcm^{-3}) the LSSM rates are roughly double the corresponding pn-QRPA rates for all temperature range shown in Table 6.

Comparing electron capture rates on ^{63}Ni, one notes from Table 7 that LSSM numbers are twice bigger at high temperature, $T_9 = 10$K, and high density, $\rho = 10^{10}$ gcm^{-3} regions. Otherwise the two calculations are in excellent agreement. Finally one notes from Table 8 that LSSM rates are roughly twice the pn-QRPA rates at all temperature-density domain shown in the table. For the case of ^{65}Ni, the pn-QRPA model calculated a total strength of magnitude 0.69 with a centroid around 1.84 MeV in daughter ^{65}Co. It is to be noted that during the presupernova phase of massive stars the LSSM electron capture rates on ^{63,65}Ni are roughly twice the pn-QRPA calculated rates.

4 Conclusions

The pn-QRPA model with an excellent track record of calculating terrestrial half-lives was used to calculate electron capture and positron decay rates on astrophysically important isotopes of nickel in stellar matter. A judicious choice of Gamow-Teller strength parameters and use of experimental deformation parameter for the even-even isotopes of nickel lead to an improved calculation of the GT strength distributions for nickel isotopes. The Ikeda sum rule was satisfied in the calculation and reasonable agreement was achieved with the measured GT$_+$ centroids for the even-even nickel isotopes. The finite temperature GT strength distributions for all nickel isotopes were also calculated.

The positron decay rates of nickel isotopes are orders of magnitude smaller than competing electron capture rates (except for the case of ^{57}Ni) and can be safely neglected in collapse simulations. The positron decay rates of ^{57}Ni competes well with the electron capture rates only during the silicon burning phases of massive stars. It was further shown that for stellar temperatures, $T_9 > 3$K, electron captures on odd-A isotopes of nickel, ^{57,59,61,63}Ni, have dominant contributions from parent excited states. Excited states contribute effectively for all isotopes of nickel during presupernova phase of massive stars and beyond.

The electron capture rates on astrophysically important odd-A isotopes were also compared with the LSSM calculation. For the case of ^{61,63}Ni the two calculations are in excellent agreement except at high densities ($\rho \sim 10^{10}$gcm^{-3}) where pn-QRPA rates are roughly half the corresponding LSSM rates. The LSSM electron capture rates on ^{65}Ni is twice the pn-QRPA rates. During silicon burning phases of massive stars, the pn-QRPA calculated electron capture

rates on ^{57,59}Ni are around an order magnitude bigger whereas during presupernova phases the calculated capture rates on ^{63,65}Ni are half of the LSSM rates. Collapse simulators are urged to take note of these comparisons for a fine tuning of the lepton-to-baryon factor (and its time rate) which is one of the key factors controlling the dynamics of core-collapse.

Acknowledgments

The author wishes to acknowledge the support of research grant provided by the Higher Education Commission, Pakistan, through HEC Project No. 20-1283.

References

1. K. Ikeda, S. Fujii and J. I. Fujita, Phys. Lett. **3**, 271 (1963).
2. C. Gaarde et al., Nucl. Phys. **A334**, 334 (1980).
3. F. Osterfeld, Rev. Mod. Phys. **64**, 491 (1992).
4. H. A. Bethe, Rev. Mod. Phys. **62**, 801 (1992).
5. G. M. Fuller, W. A. Fowler, and M. J. Newman, Astrophys. J. Suppl. Ser **42**, 447 (1980); **48**, 279 (1982); Astrophys. J.**252**, 715 (1982); **293**, 1 (1985).
6. M. B. Aufderheide, S. D. Bloom, D. A. Ressler and G. J. Mathews, Phys. Rev. C **47**, 2961 (1993); **48**, 1677 (1993).
7. J.-U. Nabi and H. V. Klapdor-Kleingrothaus, At. Data Nucl. Data Tables **71**, 149 (1999).
8. K. Langanke K. and G. Martínez-Pinedo Nucl. Phys. **A673**, 481 (2000).
9. M. B. Aufderheide, I. Fushiki, S. E. Woosley, E. Stanford and D. H. Hartmann, Astrophys. J. Suppl. Ser **91**, 389 (1994).
10. A. Heger, S. E. Woosley, G. Martínez-Pinedo, K. Langanke, Astrophys. J. **560**, 307 (2001).
11. J.-U. Nabi and M.-U. Rahman, Phys. Lett. B **612**, 190 (2005).
12. J. A. Halbleib and R. A. Sorensen, Nucl. Phys. **A98**, 542 (1967).
13. J. Krumlinde and P. Möller, Nucl. Phys. **A417**, 419 (1984).
14. K. Muto, E. Bender, T. Oda and H. V. Klapdor, Zeit. Phys. A **341**, 407 (1992).
15. A. Staudt, E. Bender, K. Muto, and H. V. Klapdor-Kleingrothaus, At. Data Nucl. Data Tables **44**, 79 (1990).
16. M. Hirsch, A. Staudt, K. Muto, and H. V. Klapdor-Kleingrothaus, At. Data Nucl. Data Tables **53**, 165 (1993).
17. J. Rapaport et al., Nucl. Phys. **A410**, 371 (1983).
18. A. L. Williams et al., Phys. Rev. C **51**, 1144 (1995).
19. M. Hagemann et al., Phys. Lett. B **579**, 251 (2004).
20. A. L. Cole et al., Phys. Rev. C **74**, 034333 (2006).
21. M. Sasano et al., Phys. Rev. C **79**, 024602 (2009).
22. N. Anantaraman et al., Phys. Rev. C **78**, 065803 (2008).
23. L. Popescu et al., Phys. Rev. C **75**, 054312 (2007).
24. L. Popescu et al., Phys. Rev. C **79**, 064312 (2009).
25. I. Stetcu and C. W. Johnson, Phys. Rev. C **69**, 024311 (2004).
26. S. Raman, C. H. Malarkey, W. T. Milner, C. W. Nestor Jr., and P. H. Stelson, At. Data Nucl. Data Tables **36**, 1 (1987).
27. P. Möller and J. R. Nix, At. Data Nucl. Data Tables **26**, 165 (1981).
28. G. Audi, A. H. Wapstra, and C. Thibault, Nucl. Phys. **A729**, 337 (2003).
29. J.-U. Nabi and H. V. Klapdor-Kleingrothaus, At. Data Nucl. Data Tables **88**, 237 (2004).
30. J. Pruet and G. M. Fuller, Astrophys. J. Suppl. Ser. **149**, 189 (2003).
31. J.-U. Nabi, Eur. Phys. J. A **40**, 223 (2009).

Table 1. Calculation of the total $S_{\beta\pm}$ strengths in nickel isotopes. The cut-off energy in daughter nuclei is 12 MeV. The second column gives the values of nuclear deformation used in the calculation.

Nucleus	Deformation	$\Sigma S_{\beta+}$	$\Sigma S_{\beta-}$
^{57}Ni	0.03558	9.98×10^{0}	$1.30\times10^{+1}$
^{58}Ni	0.18260	7.82×10^{0}	$1.38\times10^{+1}$
^{59}Ni	0.02250	5.83×10^{0}	$1.48\times10^{+1}$
^{60}Ni	0.20700	5.85×10^{0}	$1.78\times10^{+1}$
^{61}Ni	-0.09403	3.55×10^{0}	$1.85\times10^{+1}$
^{62}Ni	0.19780	3.60×10^{0}	$2.15\times10^{+1}$
^{63}Ni	-0.09203	1.73×10^{0}	$2.27\times10^{+1}$
^{64}Ni	0.17900	1.78×10^{0}	$2.57\times10^{+1}$
^{65}Ni	-0.08054	6.88×10^{-1}	$2.75\times10^{+1}$

Table 2. The pn-QRPA calculated centroids for nickel isotopes. Third and fourth columns give the corresponding values calculated by Ref. [8] and Ref. [30], respectively (values adapted from Ref. [30]). The last column shows measured values. For references see text.

Nucleus	E(GT_+)	E(GT_+) [LMP]	E(GT_+) [PF]	E(GT_+) [exp]
^{57}Ni	7.25×10^{0}	-	-	-
^{58}Ni	3.57×10^{0}	3.75×10^{0}	3.65×10^{0}	3.6 ± 0.2
^{59}Ni	5.63×10^{0}	-	-	-
^{60}Ni	3.09×10^{0}	3.40×10^{0}	2.70×10^{0}	2.4 ± 0.3
^{61}Ni	4.93×10^{0}	4.70×10^{0}	4.70×10^{0}	-
^{62}Ni	2.13×10^{0}	2.10×10^{0}	1.80×10^{0}	1.3 ± 0.3
^{63}Ni	3.73×10^{0}	-	-	-
^{64}Ni	8.00×10^{-1}	1.30×10^{0}	1.80×10^{0}	0.8 ± 0.3
^{65}Ni	1.84×10^{0}	-	-	-

Table 3. The ratios of the ground state capture rates to total capture rates, $R_{ec}(G/T)$ for isotopes of nickel. The first column gives the corresponding values of stellar temperature, T_9 (in units of 10^9 K). The ratios are calculated at density $10^{8.5} gcm^{-3}$.

$\mathbf{T_9}$	^{57}**Ni** $\mathbf{R_{ec}(G/T)}$	^{58}**Ni** $\mathbf{R_{ec}(G/T)}$	^{59}**Ni** $\mathbf{R_{ec}(G/T)}$
0.5	1.00×10^{0}	1.00×10^{0}	9.99×10^{-1}
2	8.05×10^{-1}	1.00×10^{0}	5.25×10^{-1}
3	4.70×10^{-1}	9.95×10^{-1}	2.61×10^{-1}
5	2.20×10^{-1}	9.41×10^{-1}	1.32×10^{-1}
10	1.29×10^{-1}	6.16×10^{-1}	1.42×10^{-1}
30	1.39×10^{-2}	5.68×10^{-2}	2.01×10^{-2}
	^{60}**Ni**	^{61}**Ni**	^{62}**Ni**
0.5	1.00×10^{0}	8.14×10^{-1}	4.37×10^{-2}
2	1.00×10^{0}	3.86×10^{-1}	5.30×10^{-1}
3	9.92×10^{-1}	2.68×10^{-1}	6.85×10^{-1}
5	9.26×10^{-1}	1.64×10^{-1}	6.45×10^{-1}
10	5.48×10^{-1}	1.50×10^{-1}	3.83×10^{-1}
30	4.98×10^{-2}	1.58×10^{-2}	4.34×10^{-2}
	^{63}**Ni**	^{64}**Ni**	^{65}**Ni**
0.5	1.03×10^{-1}	7.27×10^{-1}	7.55×10^{-1}
2	8.91×10^{-2}	7.16×10^{-1}	7.01×10^{-1}
3	1.11×10^{-1}	7.25×10^{-1}	6.61×10^{-1}
5	1.65×10^{-1}	6.93×10^{-1}	5.79×10^{-1}
10	1.74×10^{-1}	4.59×10^{-1}	3.31×10^{-1}
30	1.21×10^{-2}	4.66×10^{-2}	1.53×10^{-2}

Table 4. The pn-QRPA and LSSM [8] calculated electron capture rates, in units of s^{-1}, on ^{57}Ni for temperature and density domain of astrophysical interest.

T_9	pn-QRPA (10^7gcm^{-3})	LSSM (10^7gcm^{-3})	pn-QRPA (10^8gcm^{-3})	LSSM (10^8gcm^{-3})	pn-QRPA (10^9gcm^{-3})	LSSM (10^9gcm^{-3})	pn-QRPA (10^{10}gcm^{-3})	LSSM (10^{10}gcm^{-3})
2	1.95×10^{-3}	8.49×10^{-4}	4.25×10^{-2}	3.03×10^{-2}	4.28×10^{0}	7.48×10^{0}	$9.29\times10^{+2}$	$8.99\times10^{+2}$
3	7.18×10^{-3}	1.32×10^{-3}	1.15×10^{-1}	4.35×10^{-2}	5.98×10^{0}	7.82×10^{0}	$9.91\times10^{+2}$	$8.97\times10^{+2}$
5	2.91×10^{-2}	4.59×10^{-3}	3.78×10^{-1}	9.89×10^{-2}	$1.19\times10^{+1}$	8.95×10^{0}	$1.21\times10^{+3}$	$8.95\times10^{+2}$
10	4.61×10^{-1}	1.50×10^{-1}	1.86×10^{0}	6.41×10^{-1}	$3.58\times10^{+1}$	$1.65\times10^{+1}$	$1.85\times10^{+3}$	$9.89\times10^{+2}$

Table 5. Same as Table 4 but for ^{59}Ni.

T_9	pn-QRPA (10^7gcm^{-3})	LSSM (10^7gcm^{-3})	pn-QRPA (10^8gcm^{-3})	LSSM (10^8gcm^{-3})	pn-QRPA (10^9gcm^{-3})	LSSM (10^9gcm^{-3})	pn-QRPA (10^{10}gcm^{-3})	LSSM (10^{10}gcm^{-3})
2	3.06×10^{-4}	8.39×10^{-5}	6.41×10^{-3}	2.51×10^{-3}	8.13×10^{-1}	1.06×10^{0}	$4.09\times10^{+2}$	$4.26\times10^{+2}$
3	8.73×10^{-4}	1.51×10^{-4}	1.50×10^{-2}	4.02×10^{-3}	1.04×10^{0}	1.21×10^{0}	$3.77\times10^{+2}$	$4.23\times10^{+2}$
5	3.24×10^{-3}	4.95×10^{-4}	4.43×10^{-2}	1.07×10^{-2}	1.75×10^{0}	1.70×10^{0}	$3.45\times10^{+2}$	$4.31\times10^{+2}$
10	5.11×10^{-2}	3.42×10^{-2}	2.10×10^{-1}	1.50×10^{-1}	4.67×10^{0}	4.86×10^{0}	$3.86\times10^{+2}$	$4.99\times10^{+2}$

Table 6. Same as Table 4 but for ^{61}Ni.

T_9	pn-QRPA (10^7gcm^{-3})	LSSM (10^7gcm^{-3})	pn-QRPA (10^8gcm^{-3})	LSSM (10^8gcm^{-3})	pn-QRPA (10^9gcm^{-3})	LSSM (10^9gcm^{-3})	pn-QRPA (10^{10}gcm^{-3})	LSSM (10^{10}gcm^{-3})
2	5.65×10^{-7}	4.67×10^{-7}	2.65×10^{-4}	1.72×10^{-4}	9.93×10^{-2}	8.28×10^{-2}	$7.94\times10^{+1}$	$1.43\times10^{+2}$
3	7.00×10^{-6}	5.04×10^{-6}	6.14×10^{-4}	3.92×10^{-4}	1.24×10^{-1}	1.07×10^{-1}	$8.11\times10^{+1}$	$1.46\times10^{+2}$
5	9.53×10^{-5}	6.15×10^{-5}	2.25×10^{-3}	1.51×10^{-3}	1.81×10^{-1}	2.00×10^{-1}	$8.17\times10^{+1}$	$1.51\times10^{+2}$
10	5.77×10^{-3}	6.84×10^{-3}	2.47×10^{-2}	2.99×10^{-2}	6.64×10^{-1}	9.93×10^{-1}	$9.71\times10^{+1}$	$1.79\times10^{+2}$

Table 7. Same as Table 4 but for ^{63}Ni.

T_9	pn-QRPA (10^7gcm^{-3})	LSSM (10^7gcm^{-3})	pn-QRPA (10^8gcm^{-3})	LSSM (10^8gcm^{-3})	pn-QRPA (10^9gcm^{-3})	LSSM (10^9gcm^{-3})	pn-QRPA (10^{10}gcm^{-3})	LSSM (10^{10}gcm^{-3})
2	2.90×10^{-12}	4.30×10^{-12}	4.44×10^{-9}	6.10×10^{-9}	4.81×10^{-3}	5.70×10^{-3}	$2.30\times10^{+1}$	$4.98\times10^{+1}$
3	2.72×10^{-9}	3.44×10^{-9}	4.39×10^{-7}	5.21×10^{-7}	7.03×10^{-3}	7.62×10^{-3}	$2.34\times10^{+1}$	$4.98\times10^{+1}$
5	1.10×10^{-6}	1.37×10^{-6}	3.29×10^{-5}	3.97×10^{-5}	1.51×10^{-2}	1.81×10^{-2}	$2.58\times10^{+1}$	$5.28\times10^{+1}$
10	9.08×10^{-4}	1.59×10^{-3}	4.02×10^{-3}	7.00×10^{-3}	1.40×10^{-1}	2.50×10^{-1}	$4.17\times10^{+1}$	$7.48\times10^{+1}$

Table 8. Same as Table 4 but for ^{65}Ni.

T_9	pn-QRPA (10^7gcm^{-3})	LSSM (10^7gcm^{-3})	pn-QRPA (10^8gcm^{-3})	LSSM (10^8gcm^{-3})	pn-QRPA (10^9gcm^{-3})	LSSM (10^9gcm^{-3})	pn-QRPA (10^{10}gcm^{-3})	LSSM (10^{10}gcm^{-3})
2	1.87×10^{-17}	3.69×10^{-17}	2.94×10^{-14}	5.51×10^{-14}	2.47×10^{-7}	3.71×10^{-7}	7.05×10^{0}	$1.19\times10^{+1}$
3	1.25×10^{-12}	2.55×10^{-12}	2.13×10^{-10}	4.14×10^{-10}	9.44×10^{-6}	1.46×10^{-5}	6.89×10^{0}	$1.21\times10^{+1}$
5	1.41×10^{-8}	3.26×10^{-8}	4.46×10^{-7}	9.93×10^{-7}	3.19×10^{-4}	5.93×10^{-4}	7.05×10^{0}	$1.35\times10^{+1}$
10	1.12×10^{-4}	2.89×10^{-4}	5.04×10^{-4}	1.28×10^{-3}	2.00×10^{-2}	4.72×10^{-2}	$1.07\times10^{+1}$	$2.19\times10^{+1}$

Fig. 1. Gamow-Teller strength distributions in ^{57,58,59}Ni. The abscissa represents energy in cobalt isotopes.

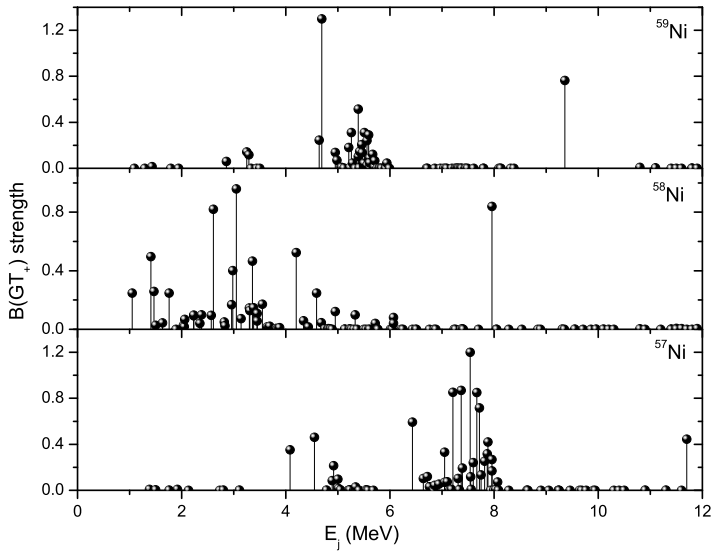

Fig. 2. Gamow-Teller strength distributions in ^{60,61,62}Ni. The abscissa represents energy in cobalt isotopes.

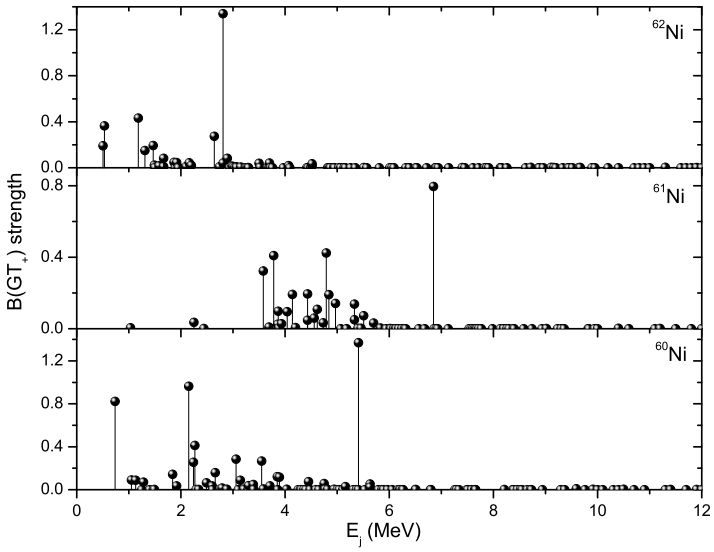

Fig. 3. Gamow-Teller strength distributions in ^{63,64,65}Ni. The abscissa represents energy in cobalt isotopes.

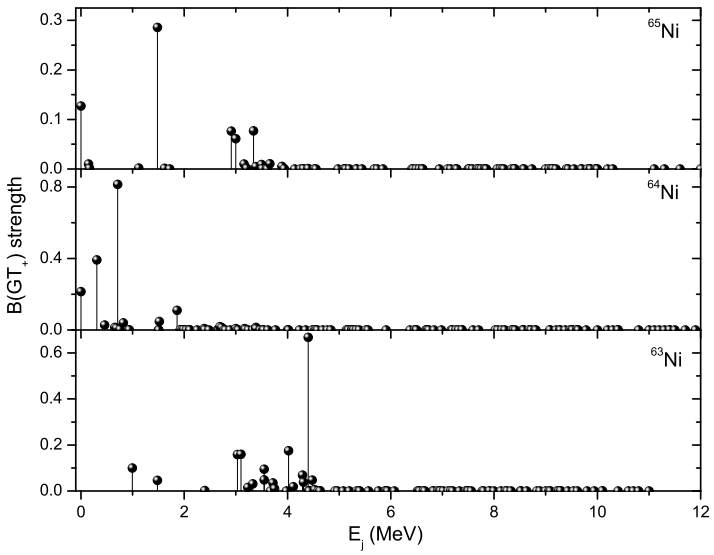

Fig. 4. (Color online) Electron capture and positron decay rates on ^{57,58,59,60}Ni as a function of stellar temperature and density. All rates are given in units of s^{-1}. Densities are given in units of gcm^{-3} and temperatures in units of 10^9 K.

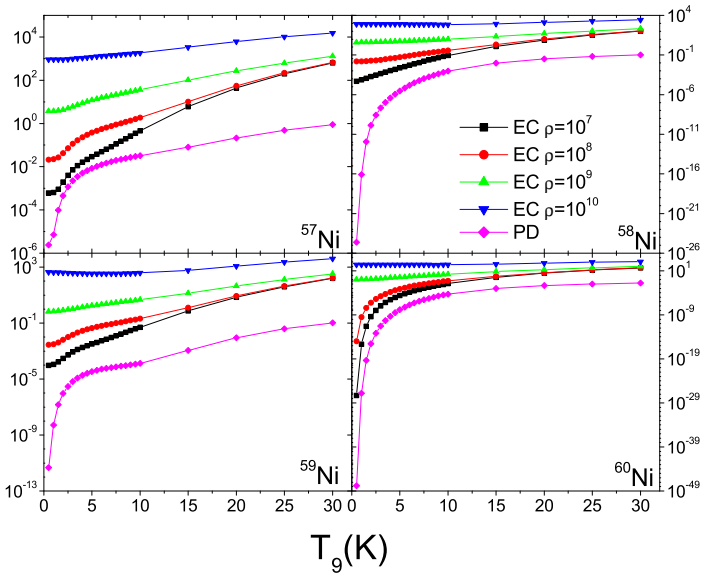

Fig. 5. (Color online) Electron capture and positron decay rates on ^{61,63,64,65}Ni as a function of stellar temperature and density. All rates are given in units of s^{-1}. Densities are given in units of gcm^{-3} and temperatures in units of 10^9 K.

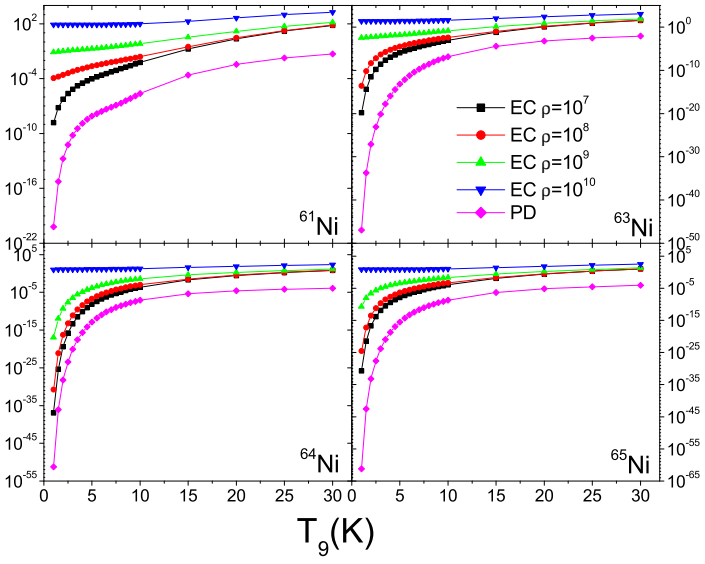

Fig. 6. (Color online) Half-lives for nickel isotopes as a function of stellar temperature calculated at a density of $\rho = 10^{8.5}$ gcm^{-3}.